Site-Selective X-Ray Absorption Fine Structure (XAFS) Spectroscopy. (1) Design of Fluorescence Spectrometer and Emission Spectra

Yasuo Izumi,* Hiroyuki Oyanagi,† and Hiroyasu Nagamori

Department of Environmental Chemistry and Engineering, Interdisciplinary Graduate School of Science and Engineering, Tokyo Institute of Technology, 4259 Nagatsuta, Midori-ku, Yokohama 226-8502

†Electrotechnical Laboratory, 1-1-4 Umezono, Tsukuba 305-8568

(Received April 14, 2000)

A Rowland-type fluorescence spectrometer was designed to measure site-selective XAFS spectra by utilizing the chemical shift of emission peak for each site. The positions of Johansson-type cylindrically-bent Ge(111) crystal and scintillation counter were controlled independently by five-channel stepping motors, thereby satisfying precise Rowland condition. Thus, measurements of many fluorescence lines over wide ranges of Bragg angle 55.6—83.9° and Rowland radius 127.7—240.9 mm are made feasible. The Cu Kα peak shifted by +1.6 eV on going from Cu to CuCl and by −0.6 eV on going from CuCl to $CuCl_2$. The Cr Kβ_1 peak shifted by +0.8 eV on going from Cr to Cr_2O_3 and by −1.6 eV on going from Cr_2O_3 to K_2CrO_4. The FWHM of Cu Kα peaks was as small as 3.0 eV. The major factor to control the energy resolution of this spectrometer was found to be geometrical angle width (slit size). The effects of Rowland radius and X-ray penetration depth into the bent crystal were smaller in the range of slit size in this paper [slit length (horizontal) in front of I_0 ion chamber was 0.5—2.0 mm and two slit lengths (vertical) in Rowland circle were 0.5—5.5 mm].

XAFS spectroscopy has been widely applied to clarify the local structure of materials[1] and biological samples.[2] EXAFS (extended X-ray absorption fine structure) gives bond distances and the coordination numbers of sites. When the sample consists of more than one kind of site, obtained values by EXAFS are the average for all sites in the sample. Heterogeneous catalysts are typical examples that consist of several kinds of sites.[3—5] XANES (X-ray absorption near-edge structure) is measured by the same method as EXAFS, and has the same problem related to the determination of electronic states of sites.

Several approaches have been taken to overcome the disadvantage of XAFS. The combination of XANES and EXAFS is used to determine the local structure and electronic state for a set of sites. The uncertainty of EXAFS curve-fitting analysis for a complex system is reduced by the complementary XANES spectra as fingerprints. Copper K-edge XANES was used to discriminate various geometries of Cu sites.[6,7] Factor analysis was used to discriminate each site among some phases of Cu–Pd/zeolite XANES.[8]

The approach of this paper is to discriminate each site (species or state of X-ray absorbing atom) experimentally for catalysts that consist of more than one kind of site. A fluorescence spectrometer was designed to analyze fluorescence X-rays from samples in the XAFS measurements. The chemical shifts[9] have been reported for Al,[10,11] P,[11] S,[11] Cl,[11] Ca,[12,13] Ti,[12,13] V,[12] Cr,[12—14] Mn,[12,13,15—18] Fe,[11—14] Co,[12] Ni,[12] and Cu.[19] The major factors to control chemical shifts of Kα and Kβ emission peaks are valence state of site, coordination number, and site symmetry.[12] XAFS spectra will be site-selective (selection of species or state for the X-ray absorbing atom) when the fluorescence spectrometer is tuned to the Kα or Kβ peak energy corresponding to each site. The difference of emission spectra by changing the excitation energy was studied.[20] The feasibility of site-selective XAFS at the Mn K-edge[21] and spin-selective XAFS at the Fe[22—24] and Mn K-edge[16,24,25] by tuning the emission energy was reported. The application of site-selective XAFS to heterogeneous catalysts is expected to allow one to explore the surface active site among coexisting inactive sites.

For example, supported Cr/SiO_2 catalysts consist of monochromate, dichromate, and polychromate Cr^{VI} species, the corresponding reduced Cr^{III} or Cr^{II} species, and cluster phases similar to α-Cr_2O_3.[26,27] It is important to obtain the relative population and structural information of Cr^{VI}, Cr^{III}, and Cr^{II} sites separately to observe the surface active site which is changing between Cr^{VI} and Cr^{III} (or Cr^{II}) during catalysis. Supported Cu/ZnO catalysts consist of several sites of Cu^0 and Cu^I in reaction conditions.[7] The reaction mechanism from CO (and/or CO_2) and H_2 to methanol is still controversial. Independent spectroscopic study of Cu^0 and Cu^I sites (geometric and electronic structures) should help the mechanistic understanding.

Herein, the design of fluorescence spectrometer and emission spectra are reported. The chemical shifts of Cu Kα and Cr Kβ peaks were evaluated. The energy resolution of this spectrometer was estimated, and factors to determine the energy resolution (incident beam size, slits size of spectrometer, Bragg angle, Rowland radius, etc.) are investigated. Site-selective XAFS spectra of Cu and Cr catalysts were reported

in Ref. 28.

Experimental

Sample Preparation. CuCl, $CuCl_2$, Cr_2O_3, and K_2CrO_4 were used as received from Wako. The Cu and Cr foils were purchased from Nilaco. Powder samples were diluted with boron nitride to a concentration of 15% copper or chromium (w/w). Each powder sample was pressed into a disk (ϕ = 20 mm).

Design of Fluorescence Spectrometer. Our fluorescence spectrometer was designed to realize high energy resolution. Higher Bragg angle and higher order reflection lead to high energy resolution, but an ordinary fluorescence spectrometer does not cover the Bragg angle range of 70—84°. The configuration of our fluorescence spectrometer to realize these factors is illustrated in Fig. 1. Each sample is placed on a plane slightly tilted from horizontal plane and the Rowland circle is in the vertical plane. A prototype of Rowland-type fluorescence spectrometer was reported equipped with spherically-bent Johann-type Si(440) crystal for high energy resolution study.[29] The six curved-crystals array fluorescence spectrometer was applied to low concentration (30—1000 ppm) metalloproteins.[24] The spectrometer in this paper was designed (1) for absorption edge atom of 1—15 wt% in catalyst; (2) to be applicable to many fluorescence lines at high Bragg angles by frequently-prepared Ge or Si crystal-face diffractions (Cr $K\beta$ at Bragg angle θ_B = 73.2° by Ge(333), Mn $K\beta$ at θ_B = 72.8° by Ge(440), Co Kβ at θ_B = 83.0° by Ge(444), Ni $K\beta$ at θ_B = 73.1° by Si(444), Cu $K\beta$ at θ_B = 79.9° by Ge(800), Mn $K\alpha$ at θ_B = 74.9° by Ge(333), Fe $K\alpha$ at θ_B = 75.5° by Ge(440), and Cu $K\alpha$ at θ_B = 79.3° by Si(444) reflections, etc.); and (3) to be applicable to high energy resolution and site-selective XAFS studies.

In the goniometer in Refs. 24 and 29, bent crystal(s) rotates and the detector moves translationally (or a fixed position-sensitive detector is used). The fluorescence spectrometer in this paper has additional position control of y-direction for crystal and y-direction and rotation for detector (Fig. 1) to realize more precise Rowland condition and thereby achieve higher energy resolution. Free choice of bent crystals of different Rowland radii enables the measurements at many fluorescence lines in a common goniometer. Emission and XAFS measurements in this paper and Ref. 28 deal with catalysts of edge atom concentration 5—15 wt%. A single bent crystal goniometer was chosen instead of multiple curved-crystals array goniometer. Beam spot size at detector was reported by three curved-crystals array (3.8×8.5 mm^2, FWHM) compared to by single crystal (1.5×2.1 mm^2, FWHM).[24] When the target is higher energy resolution and site-selective XAFS, the single crystal goniometer may be better for samples of relatively high concentration.

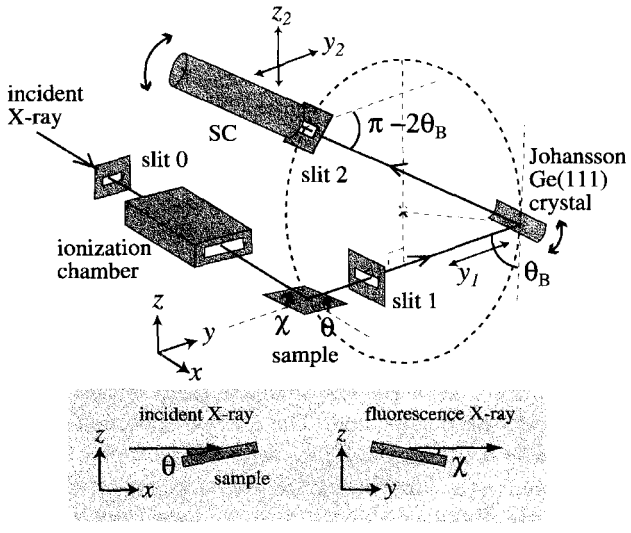

Fig. 1. Configuration of fluorescence spectrometer.

Foil or disk samples were set on a sample holder. The height of the sample holder was controlled by a micrometer to set the center of sample surface at the incident X-ray beam. The top surface of sample holder can be tilted by micrometer to the direction of the incident X-ray from the horizontal plane (angle θ; see the illustration at bottom, left in Fig. 1) to obtain an effective beam spot on the sample. The angle θ was fixed to be 6°. When the slit size in front of the I_0 ion chamber (slit 0) was 2.0 (H)×1.0 (V) mm^2, the beam spot on sample was 2.0×9.6 mm^2. The sample top surface can be tilted by micrometer also to the direction perpendicular to incident X-ray and in the same horizontal plane (angle χ; see the illustration at bottom, right in Fig. 1). The angle χ was fixed to be 7° toward bent Ge(111) crystal based on the emitted X-ray intensity dependence on the angle (see the Results section).

Cylindrically-bent Johansson-type Ge(111) crystal (50 (H)×25 (V) mm^2, R = 220(±1) mm; Crismatec, France) moves in the direction perpendicular to the incident X-rays (y-direction) and rotates by PC control. The vertical side (25 mm) of crystal is bent. The height of the center is constantly in the same plane as the center of the sample and the incident X-rays. Background noise will be smaller than fluorescence X-rays to the direction which contains fewer scattered X-rays. The geometry of θ = 6° and χ = 7° is superior to frequently-used geometry of beam entrance 45° and exit 45° in terms of signal/noise ratio. XAFS spectrum shape dependence on $\sin\theta/\sin\chi$ value was suggested for fluorescence XAFS based on theory and edge shape comparison.[30]

The scintillation counter (SC, SP-10) and the slit in front of SC (slit 2) move both in y- and z-directions and rotate by PC control. The centers of sample, bent crystal surface, and slit 2 were always on the Rowland circle during each spectrum scan (Fig. 1). Relative to the center of sample, the centers of the bent crystal surface and the slit 2 move on (0, $2R\sin\theta_B$, 0) and (0, $2R\sin\theta_B(1+\cos 2\theta_B)$, $2R\sin\theta_B\sin 2\theta_B$), respectively. Independent multichannel stepping motors (Kohzu) PC control enables free choice of bent crystals of different Rowland radii and measurements with wide ranges of Bragg angle 55.6—83.9° and Rowland radii 127.7—240.9 mm, in contrast to traditional R-$2R$ bar-type fluorescence spectrometer. This range of Bragg angle covers $K\alpha$ and $K\beta$ lines of K–As by the relatively simple index reflections of Si or Ge crystal face. The Rowland radius was fixed to be 220 mm in homemade PC software in this paper and Ref. 28.

A slit is placed between sample and bent crystal, 100 mm apart from the sample (slit 1). The configuration in Fig. 1 effectively focuses the divergence which originated from the incident X-ray beam (polarized horizontally). An alternative spectrometer configuration is vertical sample and horizontal Rowland-circle plane, to effectively focus incident X-ray beam divergence. The reasons why vertical Rowland configuration was chosen in this work are easy sample holding (e.g., powder and elastic or breakable disk on nearly horizontal plane) and the possibility of extension to surface sensitive study[31] because small-angle X-ray incidence on sample is only possible for our configuration. When a small-angle incident X-ray makes a spot on a sample placed vertically, the horizontal width of the spot becomes longer and a big bent crystal will be necessary.

Obtained emission spectra were found to have significant background due to scattered X-rays from the air. To escape from such

effects, 1 mm-thick lead plates completely covered the sample except for primary beam entrance and fluorescence X-ray beam exit toward bent crystal (Fig. 1). Most of the data in this paper were obtained without a lead shield, and the spectrum obtained with lead shield is compared with the others to clarify the scattered X-ray effects from the air.

To cancel the effects of gravity, the position of the bent crystal (x, y, and z and the rotation around the axis in the crystal surface and perpendicular to the θ_B rotation axis) was adjusted by four micrometers, maximizing the fluorescence X-ray intensity at SC. The I_0 ion chamber, sample holder, bent crystal, SC, and slits are on a table and covered by an acrylic house.

Emission Spectrum Measurements. Cu $K\alpha$ and Cr $K\beta$ emission spectra were measured at bending-magnet beamline 7C of KEK-PF (the Photon Factory in the National Laboratory for High Energy Physics) (Proposal Nos. 99G060 and 98P025). The storage ring energy was 2.5 GeV and the ring current was 380—260 mA. The ring emittance was 36 nm rad. A Si(111) double crystal monochromator was used. The incident X-ray beam was focused by a sagittal focusing mechanism and fully tuned by a Piezo translator. Cu $K\alpha$ emission spectra were also measured at Undulator beamline 10XU of SPring8 (Proposal No. 1999B0220-NX-np). The storage ring energy was 8.0 GeV and the ring current was 99—74 mA. The ring emittance was 7 nmrad. Si(111) double crystal monochromator was used. The Undulator gap[32] and the Piezo translator were controlled during each step of spectrum scan to optimize to the I_0 beam intensity.[33]

The I_0 beam was monitored by an ion chamber filled with nitrogen for the Cu samples and filled with a mixture of helium (70%) and nitrogen (30%) for the Cr samples. The sample was at room temperature.

Cu $K\alpha$ emission was monitored with Ge(444) reflection. The atmosphere in the acrylic house of spectrometer was air. The incident X-ray energy (excitation energy) was 9000.1 eV. The high voltage of SC was 1000 V. The spectrum scan step was 0.01° of Bragg angle (ca. 0.5 eV) and an emission spectrum consists of 80 steps. The accumulation time of a step was 60 s. Cr $K\beta$ emission was monitored with Ge(333) reflection. The atmosphere in acrylic house was purged with helium, minimizing the extinction of X-rays. The excitation energy was 6020.9 eV. The high voltage of SC was 600 V to prevent the discharge of SC in helium. The spectrum scan step was 0.01° of Bragg angle (ca. 0.3 eV) and an emission spectrum consists of 120 steps. The accumulation time of a step was 60 s.

Obtained emission spectra were fitted with Gaussian functions + flat background. Based on the fitting, energy position and FWHM (full width at a half maximum) of peaks were evaluated. The energy was calibrated by equalizing Cu foil $K\alpha_1$ peak top to 8047.8 eV or Cr foil $K\beta_1$ peak top to 5946.7 eV.[34] The peak energy positions were reproduced within 0.3 and 0.2 eV when several spectra were scanned for Cu $K\alpha$ and Cr $K\beta$, respectively.

Results

Emitted X-Ray Intensity vs. Angle χ. X-Rays emitted from samples were monitored by SC temporarily placed between slit 1 and bent crystal (Fig. 1) when the incident X-ray energy was 8958.4 and 9000.1 eV (below and above Cu K-edge, respectively) for $CuCl_2$. The emitted X-ray intensity dependence on the angle χ is shown in Fig. 2a. The difference between the two curves estimates Cu $K\alpha$ fluorescence X-ray intensity.[35] The intensity difference increased

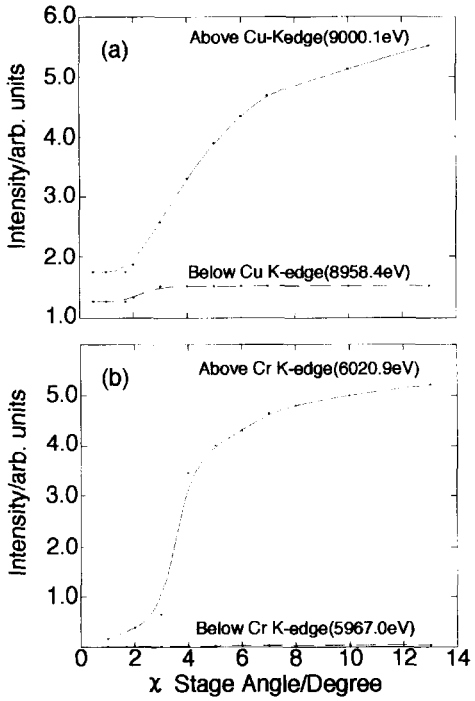

Fig. 2. The dependence of X-ray intensity emitted from the sample on angle χ. The excitation energies were below and above the Cu K-edge for $CuCl_2$ (a) and below and above the Cr K-edge for Cr/SiO_2 catalyst (b).

at 2° and began to saturate at > 10°. As the sample is a disk pressed from powder, emitted fluorescence X-ray from sample surface may be absorbed again into the sample when the angle χ is as small as 0—3°. Corresponding data for Cr/SiO_2 sample, when the incident X-ray energy was 5967.0 and 6020.9 eV, are drawn in Fig. 2b. The fluorescence X-ray intensity increased at 3° and began to saturate at ca. 10°. Based on these data (intensity) and signal/noise dependence on the angle (see the Experimental section), all the emission spectra were observed with the angle χ of 7°.

Cu $K\alpha$ Emission Spectra. Cu $K\alpha$ emission spectra were measured for Cu foil, CuCl, and $CuCl_2$. The spectra are shown in Fig. 3 and peak energies and FWHM are listed in Table 1a. Two peaks $K\alpha_2$ and $K\alpha_1$ were observed, and the intensity ratio was about 1 : 2. The energy splitting of the two peaks was 19.6 eV, similar to the value in the reference (19.8 eV).[36] The peak top in ref. 36 was determined by four peaks fitting ($K\alpha_1$ + side peak, $K\alpha_2$ + side peak). Data in Table 1a are based on one Gaussian fitting for one peak. The difference of peak number for fitting may be the reason for different values of splitting. When the Cu foil was shielded by lead plates, the background level in Fig. 3a reduced to nearly zero in Fig. 3a′ and signal/noise ratio was dramatically improved.

The peak energy shifted by +1.6 eV on going from Cu^0 to Cu^I and by −0.6 eV on going from Cu^I to Cu^{II} both for $K\alpha_1$ and $K\alpha_2$ peaks (Table 1a). The FWHM values of $K\alpha_1$ and $K\alpha_2$ peaks were nearly the same for each compound.

Next, slit size effects on the FWHM were investigated for Cu foil in relation to the energy resolution of fluorescence

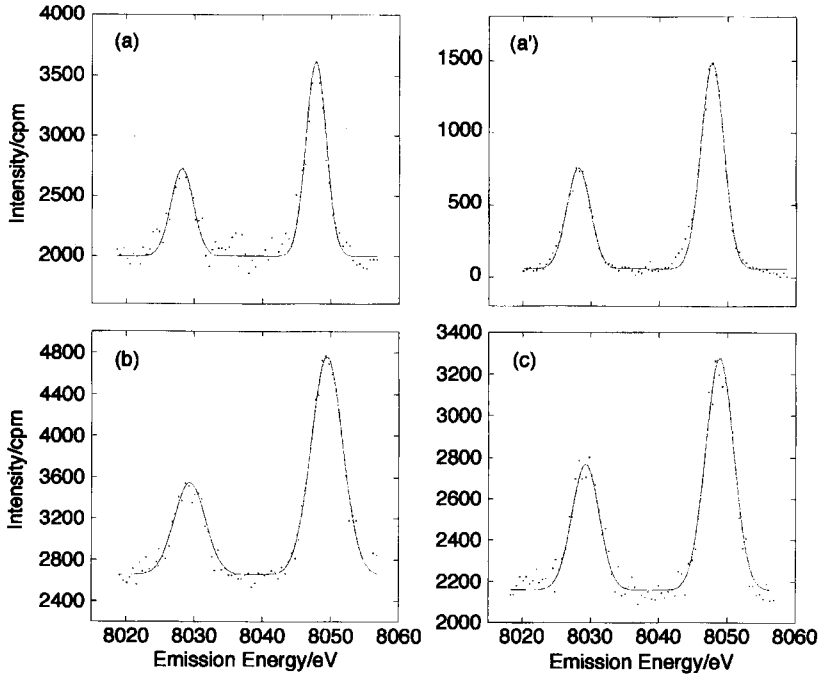

Fig. 3. Cu $K\alpha$ emission spectra of Cu foil (a, a'), CuCl (b), and $CuCl_2$ (c). The experimental data are plotted as points and the Gaussian fittings are drawn as solid lines. These spectra correspond to Table 1a. The sample was shielded by lead plates for (a').

Table 1. Peak Energies and FWHM of Cu $K\alpha_1$ and $K\alpha_2$ (a) and Cr $K\beta_1$ and $K\beta'$ (b) in the Emission Spectra

(a) Cu $K\alpha$ emission

Sample	Peak energy/eV			FWHM/eV	
	$K\alpha_1$	$K\alpha_2$	Split	$K\alpha_1$	$K\alpha_2$
Cu Foil	8047.8	8028.2	19.6	3.5	3.7
CuCl	8049.4	8029.8	19.6	5.4	5.3
$CuCl_2$	8048.8	8029.2	19.6	4.8	4.7

(b) Cr $K\beta$ emission

Sample	Peak energy/eV			FWHM/eV	
	$K\beta_1$	$K\beta'$	Split	$K\beta_1$	$K\beta'$
Cr foil	5946.7	5941.4	5.3	3.7	6.2
Cr_2O_3	5947.5	5939.9	7.6	6.2	6.2
K_2CrO_4	5945.9	5939.3	6.6	5.3	5.3

The size of slit 0 was 2.0(H)×1.0(V) mm^2. The size of slits 1 and 2 was 8.0(H)×2.0(V) mm^2 except for Cr_2O_3 and K_2CrO_4 [8.0(H)×5.5(V) mm^2].

Table 2. Dependence of the FWHM of Cu Foil $K\alpha$ Emission Peak on Three Slits Size

Slit size/mm^2			FWHM/eV	
Slit 0	Slit 1	Slit 2	$K\alpha_1$	$K\alpha_2$
(a) KEK-PF, 7C				
2.0×1.0	8.0×5.5	8.0×5.5	6.0	6.1
	8.0×2.0	8.0×2.0	3.5	3.7
0.5×1.0	8.0×2.0	8.0×2.0	3.3	3.5
(b) SPring8, 10XU				
2.0×1.0	8.0×2.0	8.0×2.0	5.4	5.8
	8.0×1.0	8.0×1.0	4.2	4.2
	8.0×0.5	8.0×0.5	3.0	3.0
1.0×1.0	8.0×1.0	8.0×1.0	3.5	3.6
0.5×1.0	8.0×1.0	8.0×1.0	3.4	3.4

Slit size: Horizontal length by vertical length.

spectrometer. The size of slits 1 and 2 was varied at the same time. When the length(V) of slits 1 and 2 decreased from 5.5 to 2.0 mm [length(H) 8.0 mm, slit 0 : 2.0(H)×1.0(V) mm^2] at PF, the FWHM significantly decreased from 6.0 (±0.1) to 3.6 (±0.1) eV (Table 2a). When the length(H) of slit 0 decreased from 2.0 to 0.5 mm [length(V) 1.0 mm, slits 1 and 2 : 8.0(H)×2.0(V) mm^2], the change of FWHM was from 3.6 (±0.1) to 3.4 (±0.1) eV.

When the length(V) of slits 1 and 2 decreased from 2.0 to 1.0 and then to 0.5 mm [length(H) 8.0 mm, slit 0 : 2.0(H)×1.0(V) mm^2] at SPring8, the FWHM progressively decreased from 5.6 (±0.2) to 4.2 and then to 3.0 eV (Table 2b). When the length(H) of slit 0 decreased from 2.0 to 1.0 mm [length(V) 1.0 mm, slits 1 and 2: 8.0(H)×1.0(V) mm^2], the FWHM decreased from 4.2 to 3.5 (±0.1) eV. The decrease from the slit 0 length(H) 1.0 to 0.5 mm was smaller: from 3.5 (±0.1) to 3.4 eV. These trends reflect the incident beam size of ca. 2.0(H)×1.0(V) mm^2 at beamline 7C (focused) of PF[37] and ca. 1.0(H)×1.0(V) mm^2 at beamline 10XU of SPring8.

Unexpectedly, the energy resolution of emission spectra at PF 7C was better than that at SPring8 10XU when the size of slit 0 was 2.0(H)×1.0(V) mm^2 and that of slits 1 and 2 was 8.0(H)×2.0(V) mm^2 ($K\alpha_1$ FWHM was 3.5 and 5.4 eV, respectively; Table 2). Two possible reasons are as follows: (1) different primary beam incidence angle on sample (the angle θ in Fig. 1 is with reference to the horizontal plane), and (2) different X-ray penetration depth into sample (different effective source size in the plane of diffraction, see the Discussion section) due to the excitation of higher-

order Undulator beam. However, fluorescence X-ray counts at Cu $K\alpha_1$ top were ca. 1600 and ca. 64000 cpm (counts per a minute), respectively, at SC in the condition. The difference means that potentially better energy resolution at SPring8 10XU can be achieved by reducing the slit size of fluorescence spectrometer.

Cr $K\beta$ Emission Spectra. Cr $K\beta$ emission spectra were measured for Cr foil, Cr_2O_3, and K_2CrO_4. The spectra are shown in Fig. 4 and peak energies and FWHM are listed in Table 1b. One strong peak at 5945.9—5947.5 eV and a shoulder on lower energy side were observed in the spectra.

Three wave fits were reported for Cr $K\beta$ emission spectra.[38] Main peak, weak peak in the middle, and lower-energy weak peak were (tentatively) assigned to $K\beta_1$, $K\beta_3$, and $K\beta'$, respectively. The intensity ratio $(K\beta' + K\beta_3)/K\beta_1$ was in the order K_2CrO_4 < Cr < Cr_2O_3, and the energy difference between $K\beta_1$ and $K\beta'$ was in the order Cr (8.3) < K_2CrO_4 (10.3) < Cr_2O_3 (12.8 eV). In this work, the intensity ratio (shoulder peak)/$K\beta_1$ was in the order K_2CrO_4 < Cr < Cr_2O_3 (Fig. 4), and the energy difference of the two peaks was in the order Cr (5.3) < K_2CrO_4(6.6) < Cr_2O_3 (7.6 eV) by two wave fits (Table 1b). Similar Cr $K\beta$ emission spectra to Fig. 4a and b were reported for Cr and Cr_2O_3, where the shoulder peak on lower energy side was assigned to $K\beta'$.[13,39] Minor discrepancies between Ref. 38 and this work may be due to the differences of the number of fit functions and energy resolution. Inequivalent FWHM of $K\beta_1$ and $K\beta'$ for Cr foil (Table 1b) may be due to two functions fit. Three wave fits were tried for Fig. 4, but several possible fits were obtained for one spectrum. Theoretical peak splitting data based on multiplet calculations are necessary to perform three wave fits, similar to the simulations of Mn $K\beta$ emission spectra.[16]

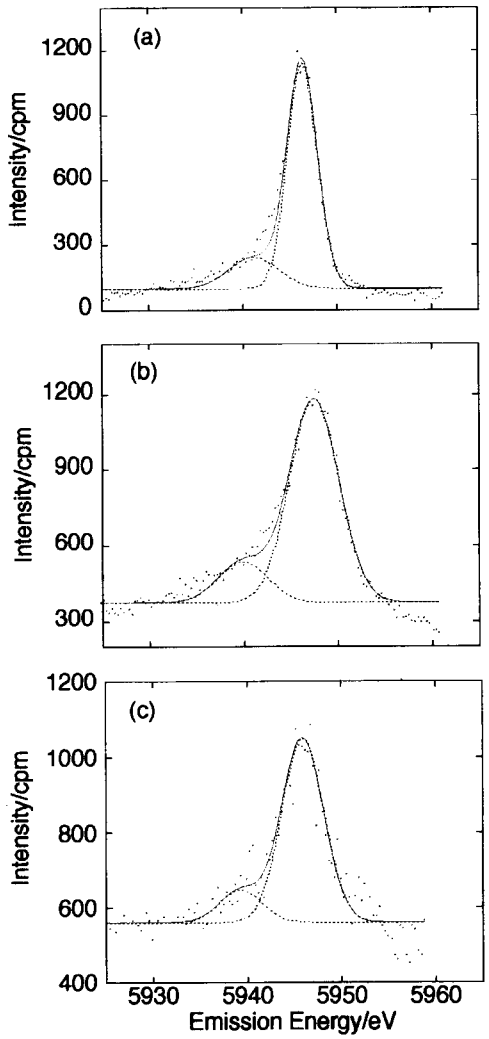

Fig. 4. Cr $K\beta$ emission spectra of Cr foil (a), Cr_2O_3 (b), and K_2CrO_4 (c). The experimental data are plotted as points and the Gaussian fittings are drawn as solid (total) and dotted (each component) lines. These spectra correspond to Table 1b. The sample was shielded by lead plates for (a).

The $K\beta_1$ peak energy shifted by +0.8 eV on going from Cr^0 to Cr^{III} and by −1.6 eV on going from Cr^{III} to Cr^{VI} (Table 1b). The FWHM of $K\beta_1$ peak for Cr foil was 3.7 eV. Background level reduced to nearly zero and the signal/noise ratio was improved when lead shield was used for Cr foil (Fig. 4a).

Discussion

Chemical Shifts of Fluorescence X-Ray Peak. Chemical shifts of fluorescence X-ray energy were reported for $K\alpha$ and $K\beta_1$ emission of Ca, Ti, V, Cr, Mn, Fe, Co, and Ni.[12] The $K\alpha_1$ chemical shifts from metallic state ranged from −0.7 eV (Ti → TiO_2) to +0.3 eV (Mn → MnO), and those of $K\beta_1$ ranged from −1.0 eV (Cr → K_2CrO_4) to +1.0 eV (Mn → MnO or MnO_2). The $K\beta_1$ chemical shifts were relatively large for Cr and Mn. The trend was nearly equivalent for $K\beta_1$ of Ca, Ti, Cr, Mn, and Fe in Ref. 13, and somewhat different for Mn $K\beta_1$ (Mn → MnO or MnO_2 +1.4 eV) in Ref. 17. Reported chemical shifts were +0.6[12] or +0.4 eV[13] on going from Cr to Cr_2O_3 and −1.6[12] or −1.4 eV[13] on going from Cr_2O_3 to K_2CrO_4. Observed chemical shifts in this paper were +0.8 eV on going from Cr to Cr_2O_3 and −1.6 eV on going from Cr_2O_3 to K_2CrO_4 (Table 1b), an acceptable level of agreement with values in reference, taking into account the reproducibility of the Kβ_1 peak energy (< 0.2 eV). The chemical shifts were +1.6 eV on going from Cu to CuCl and −0.6 eV on going from CuCl to $CuCl_2$.

In summary, the chemical shifts between Cr^{III} and Cr^{VI} and between Cu^0 and Cu^I were relatively large (ΔE = 1.6 eV), and will be utilized in site-selective XAFS measurements. Fortunately in view of catalysis, Cr^{III} and Cr^{VI} sites for Cr/SiO_2 catalysts and Cu^0 and Cu^I sites for Cu/ZnO catalysts are closely related to catalysis as active sites or synergetic (promotion) sites.[7,26]

Energy Resolution of Emission Spectra. The peak width of emission spectra is determined by several factors: incident beam size at sample, energy resolution of spectrometer, and natural lifetime of core hole for 1s and 2p (Cu $K\alpha$) or 1s and 3p (Cr $K\beta$) levels. The energy resolution of flat crystal was formulated as[40]

$$\Delta E/E = \cot\theta_B \Delta\Theta, \quad (1)$$

$$\Delta\Theta = [(\Delta\theta)^2 + (\Delta\omega)^2]^{1/2}, \quad (2)$$

where $\Delta\theta$ is the geometrical angle width, and $\Delta\omega$ is the diffraction curve width of crystal. The receiving slit size (e.g., slits 1 and 2 in Fig. 1) and Rowland radius determine $\Delta\theta$. The element of crystal and the diffraction face determine $\Delta\omega$.

$\Delta\Theta$ was formulated for bent crystal as the effects of geometrical angle width, the divergence of beam perpendicular to the Rowland circle plane, and the X-ray penetration depth into the crystal,[41]

$$\Delta\Theta = \frac{[(W_s + W_f)^2 + (h^2/8R\cos\theta_B)^2 + \{(2\cos\theta_B \sin\theta_B \ln 2)/\mu\}^2]^{1/2}}{8R \sin\theta_B}, \quad (3)$$

where W_s is the effective source size in the plane of diffraction, W_f is the slit width (vertical in Fig. 1) on Rowland circle between the bent crystal and SC, μ is the absorption coefficient of crystal, h is the slit length (horizontal in Fig. 1), and R is the Rowland radius. Then, energy resolution of bent crystal spectrometer is

$$\Delta E = E\cot\theta_B\Delta\Theta \approx \frac{E^3(2d)^2}{8RC^2} \times \left[(W_s + W_f)^2 + \left(\frac{h^2}{8R}\right)^2 + \left(\frac{CE^2\ln 2}{Kd}\right)^2\right]^{1/2}, \quad (4)$$

where E is the fluorescence X-ray energy, d is the lattice constant of crystal, and C is a constant (12.398 keV Å). K is the approximation of μE^3. First term reflects the slit size effects. Second term reflects Rowland radius effects. Smaller slit size and larger Rowland circle improve energy resolution. Third term reflects X-ray penetration effects into bent crystal. The effects become critical as the fluorescence X-ray energy increases.

The energy resolution is evaluated based on Eq. 4 when the length(H) of slit 0 was 2.0 mm. With χ of 7° (Fig. 1), effective source size at sample (W_s) is approximated: slit 0 length(H) 2.0 mm×tan 7° ca. 0.246 mm. With the length-(V) of slit 1 of 0.5 mm, the angle divergence is 0.0075.[40] Hence, ΔE is calculated to be 2.5 eV. First term was dominant. Second and third terms were smaller than first term by more than two orders of magnitude. The natural core-hole lifetime[25,42] of Cu K+L_3 levels is 2.11 eV in total.[43] The convoluted width of estimated energy resolution and natural core-hole lifetime width is ca. 2.4 eV, similar to experimental peak width of Cu $K\alpha_1$ (3.0 eV, Table 2). These similar values demonstrate that the precise Rowland condition was satisfied by multichannel independent control of bent crystal and SC (see Experimental section).

The energy resolution of Cr $K\beta$ emission spectrum is also evaluated based on Eq. 4. With the slit 0 length(H) of 2.0 mm, beam height at sample was 0.246 mm and ΔE was calculated to be 1.8 eV. Again, first term dominates. The natural core-hole lifetime of Cr K level is 1.08 eV.[43] The convoluted width of estimated energy resolution and natural core-hole lifetime width is ca. 1.5 eV, smaller than the experimental peak width of 3.7 eV (Table 1b). In general, spectrometer resolution is a little bit worse than ideal theoretical energy resolution.[41]

Incident beam size effects and slit size effects were verified by progressively changing the size of slit 0 and the size of slits 1 and 2 (Table 2). The Rowland radius and X-ray penetration depth into crystal were not primarily important in the ranges of three slits size in Tables 1 and 2 and fluorescence energy (5940—8050 eV).

Summary

A high energy-resolution fluorescence spectrometer was designed for site-selective XAFS measurements. The points of this spectrometer were individual position control of Johansson-type cylindrically-bent Ge(111) crystal and scintillation counter to enable precise Rowland condition. It enables application to many fluorescence lines due to wide ranges of Bragg angle 55.6—83.9° and Rowland radius 127.7—240.9 mm. The chemical shift was relatively large on going from Cu to CuCl (+1.6 eV) and on going from Cr_2O_3 to K_2CrO_4 (−1.6 eV).

The major factors to control the energy resolution of this fluorescence spectrometer were the length(H) of slit 0 and length(V) of slits 1 and 2 (Fig. 1). The former affected the energy resolution until it reached the beam width of beamline. According to the decrease of latter, energy resolution was progressively improved. The FWHM was as small as 3.0 eV at SPring8 10XU. The convolution of energy resolution based on a reported formula for bent-crystal spectrometer and natural core-hole lifetime width was comparable to experimental FWHM. Rowland radius and the X-ray penetration depth into bent crystal were found to be less important with respect to energy resolution within the above ranges of slit sizes and fluorescence X-ray energy.

This work was supported by grants from Toray Science Foundation (No. 98-3901, Y.I.), Kanagawa Academy of Science and Technology (No. 9991008, Y.I.), and Grants-in-Aid for Scientific Research from the Ministry of Education, Science, Sports and Culture (Nos. 08874066 and 12740376, Y.I. and 10355032, Prof. K. Aika). We thank Prof. M. Nomura (KEK-PF) and Dr. M. Ishii (SPring8) for instructions about beamlines.

References

1 Y. Iwasawa, "X-Ray Absorption Fine Structure (XAFS) for Catalysts and Surfaces," World Scientific, Tokyo (1996).

2 D. C. Koningsberger and R. Prins, "X-Ray Absorption," John Wiley & Sons, New York (1988).

3 Y. Izumi, *Trends Inorg. Chem.*, **5**, 43 (1998).

4 Y. Izumi, *Platinum Met. Rev.*, **41**, 166 (1997).

5 Y. Izumi and Y. Iwasawa, *CHEMTECH*, **24**, 20 (1994).

6 L. Kau, D. J. Spira-Solomon, J. E. Penner-Hahn, K. O. Hodgson, and E. I. Solomon, *J. Am. Chem. Soc.*, **109**, 6433 (1987).

7 L. Kau, K. O. Hodgson, and E. I. Solomon, *J. Am. Chem. Soc.*, **111**, 7103 (1989).

8 M. Fernandez-Garcia, C. M. Alvarez, and G. L. Haller, *J. Phys. Chem.*, **99**, 12565 (1995).

9 A. Meisel, G. Leonhardt, and R. Szargan, "X-ray Spectra and Chemical Binding," Springer, New York (1989).

10 E. Kallne in "Encyclopedia of Physics," Addison-Wesley Publishing Co., Reading, USA (1981), pp. 1113—1116.

11 W. T. Cave in "Handbook of X-Rays," McGraw-Hill, USA (1967), Chap. 34.1—34.3.

12 A. E. Sandstrom in "Encyclopedia of Physics," ed by S. Fluge, Springer-Verlag, Berlin (1957), Vol. 30, p. 159.

13 A. S. Koster and H. Mendel, *J. Phys. Chem. Solids*, **31**, 2511 (1970).

14 G. Leonhardt and A. Meisel, *J. Chem. Phys.*, **52**, 6189 (1970).

15 U. Bergmann, M. M. Grush, C. R. Horne, P. DeMarois, J. E. Penner-Hahn, C. F. Yocum, D. W. Wright, C. E. Dube, W. H. Armstrong, G. Christou, H. J. Eppley, and S. P. Cramer, *J. Phys. Chem.*, **102**, 8350 (1998).

16 G. Peng, F. M. F. de Groot, K. Hamalainen, J. A. Moore, X. Wang, M. M. Grush, J. B. Hastings, D. P. Siddons, W. H. Armstrong, O. C. Mullins, and S. P. Cramer, *J. Am. Chem. Soc.*, **116**, 2914 (1994).

17 K. Tsutsumi, H. Nakamori, and K. Ichikawa, *Phys. Rev. B*, **13**, 929 (1976).

18 M. Oku, H. Matsuta, K. Wagatsuma, and T. Konishi, *J. Chem. Soc., Faraday Trans.*, **92**, 2759 (1996).

19 I. I. Tupitsyn, L. L. Makarov, and J. F. Batrakov, *J. Phys. Chem. Solids*, **59**, 809 (1998).

20 P. L. Cowan, *Phys. Scr.*, **T31**, 112 (1990).

21 M. M. Grush, G. Christou, K. Hamalainen, and S. P. Cramer, *J. Am. Chem. Soc.*, **117**, 5895 (1994).

22 G. Peng, X. Wang, C. R. Randall, J. A. Moore, and S. P. Cramer, *Appl. Phys. Lett.*, **65**, 2527 (1994).

23 X. Wang, C. R. Randall, G. Peng, and S. P. Cramer, *Chem. Phys. Lett.*, **243**, 469 (1995).

24 X. Wang, M. M. Grush, A. G. Froeschner, and S. P. Cramer, *J. Synchrotron Rad.*, **4**, 236 (1997).

25 K. Hamalainen, C. C. Kao, J. B. Hastings, D. P. Siddons, L. E. Berman, V. Stojanoff, and S. P. Cramer, *Phys. Rev. B*, **46**, 14274 (1992).

26 W. Hill and G. Ohlmann, *J. Catal.*, **123**, 147 (1990).

27 B. M. Weckhuysen, R. A. Schoonheydt, J. Jehng, I. E. Wachs, S. J. Cho, R. Ryoo, S. Kijlstra, and E. Poels, *J. Chem. Soc., Faraday Trans.*, **91**, 3245 (1995).

28 Y. Izumi and H. Nagamori, *Bull. Chem. Soc. Jpn.*, **73**, 1581 (2000).

29 V. Stojanoff, K. Hamalainen, D. P. Siddons, J. B. Hastings, L. E. Berman, S. Cramer, and G. Smith, *Rev. Sci. Instrum.*, **63**, 1125 (1992).

30 J. M. Lee, H. H. Yoo, and M. Joo, *J. Synchrotron Rad.*, **6**, 244 (1999).

31 H. Oyanagi, *Appl. Surf. Sci.*, **60/61**, 522 (1992).

32 H. Oyanagi, M. Ishii, C. Lee, N. L. Saini, Y. Kuwabara, A. Saito, Y. Izumi, and H. Hashimoto, *J. Synchrotron Rad.*, **6**, 155 (1999).

33 Control software was written by Dr. H. Tanida, SPring8.

34 J. A. Bearden, *Rev. Mod. Phys.*, **39**, 78 (1967).

35 J. Stohr, "NEXAFS Spectroscopy," Springer, New York (1992), p. 133.

36 M. Deutsch, G. Holzer, J. Hartwig, J. Wolf, M. Fritsch, and E. Forster, *Phys. Rev. A*, **51**, 283 (1995).

37 M. Nomura, A. Koyama, and M. Sakurai, *KEK Report*, **91-1**, 1 (1991).

38 K. Tsutsumi and H. Nakamori, *J. Phys. Soc. Jpn.*, **25**, 1418 (1968).

39 B. Ekstig, E. Kalline, E. Noreland, and R. Manne, *Phys. Scr.*, **2**, 38 (1970).

40 H. Oyanagi, "The Basics of Synchrotron Radiation," Maruzen, Tokyo (1996).

41 P. Georgopoulos and G. S. Knapp, *J. Appl. Crystallogr.*, **14**, 3 (1981).

42 P. H. Citrin, P. M. Eisenberger, W. C. Marra, T. Aberg, J. Utriainen, and E. Kallne, *Phys. Rev. B*, **10**, 1762 (1974).

43 M. O. Krause and J. H. Oliver, *J. Phys. Chem. Ref. Data*, **8**, 329 (1979).